# Supporting Information

# Boosting Toluene Combustion by Engineering Co-O Strength in Cobalt Oxide Catalysts

*Yongjie Shen,[1‡] Jiang Deng,[1‡] Sarawoot Impeng,[2‡] Shuangxi Li,[1] Tingting Yan,[1] Jianping Zhang,[1] Liyi Shi,[1] and Dengsong Zhang[1]**

[1]State Key Laboratory of Advanced Special Steel, School of Materials Science and Engineering, International Joint Laboratory of Catalytic Chemistry, Department of Chemistry, Research Center of Nano Science and Technology, College of Sciences, Shanghai University, Shanghai 200444, China.

[2]National Nanotechnology Center, National Science and Technology Development Agency, 12120 Pathum Thani, Thailand.

‡These authors contributed equally to this work.

*whom correspondence should be addressed. E-mail: dszhang@shu.edu.cn

Phone: + 86-21-66132793

This Supporting Information contains:

Total number of pages: 35

Total number of tables: 5

Total number of figures: 19

CONTENTS

## CHARACTERIZATIONS

X-ray diffraction (XRD) patterns were recorded using 3KW D/MAX-2500 X-ray diffractometer equipped with Cu Kaα radiation at 40 kV and 140 mA at a scanning rate of 8° $min^{-1}$. Thermogravimetric analysis (TGA) was conducted on a Thermogravimetric Analyzer (SHIMADZU DTG-60H), at a rate of 10 °C $min^{-1}$ under air flow. Raman measurements were carried out at room temperature, and the signals were recorded by FT-Raman spectrophotometer (LabRAM HR Evolution, Bruker). An Nd:YAG laser 633 nm line was used as the excitation source. The obtained XPS spectra were recorded with a resolution of approximately 1.5. X-ray photoelectron spectrum (XPS) analysis was conducted with a VG SCIENTA R3000 X-ray photoelectron spectroscope equipped with Al Kα radiation, and the binding energy was calibrated by the C 1s peak (284.8 eV) of contamination carbon. Specific surface area ($S_{BET}$) was calculated based on $N_2$ adsorption/desorption isotherms recorded on a ASAP 2460 Surface Area and Porosity Analyzer (Micrometrics, USA), at 77 K, all samples were outgassed under vacuum at 300 °C for 12 h. SIGMA-300 field emission electron microscope (FESEM) was used to observe the morphology and particle size of the synthesized catalyst. HR-TEM observations were carried out by a high-resolution TEM (HRTEM, JEOL JEM-2100F) at 200 kV. The EPR test was conducted using the Bruker A300 at low temperature.

$H_2$ temperature programmed reduction ($H_2$-TPR) was performed on an AutoChem II 2920 adsorption apparatus (Micromeritics, USA) equipped with TCD detector. Prior to $H_2$-TPR experiment, 30 mg of catalysts was pretreated with He with a total flow rate of 30 mL·$min^{-1}$ at 300 °C for 0.5 h, then cooled down to room

temperature in the He atmosphere. Finally, the reactor temperature was raised to 600 °C at a constant heating rate of 10 °C·min$^{-1}$ in a flow of $H_2$ (10 vol %)/He (30 mL·min$^{-1}$). The $H_2$ consumption during the experiment was monitored by a TCD.

Temperature programmed desorption of $O_2$ ($O_2$-TPD) was conducted on the TP2920 AutoChem adsorption analyzer. 30 mg sample was pretreated under the He atmosphere (30 mL·min$^{-1}$) at 300 °C for 30 min and cooled down to 30 °C at the same airstream condition. After the catalyst was in $O_2$(2 vol %)/He (30 mL·min$^{-1}$) at 300 °C for 0.5 h, the treated catalyst was heated from 30 °C to 800 °C with a rate of 10 °C·min$^{-1}$ in a He flow (30 mL·min$^{-1}$).

Toluene TPD-MS was tested using a TP 5080 (Xianquan, Tianjin, China) chemical adsorption instrument and an OMNISTAR (Pufa, Shanghai, China) spectrometer. 30 mg sample was pretreated at 300 °C for 0.5 hours in the He atmosphere (30 mL · min$^{-1}$), and cool to 30 °C under the same airflow conditions. After the catalyst was treated in toluene (1000ppm) / He (50 mL · min$^{-1}$) for 1 hour, it was purged with He gas for 0.5 hours. Then the treated catalyst was heated from 30 °C to 600 °C in He gas (30 mL · min$^{-1}$) at a rate of 5 °C.

FTIR and operando/ in-situ DRIFTS experiments were carried out on a Nicolet is50 spectrometer (Thermo Fisher, USA) equipped with a Harrick DRIFTS cell and an MCT/A detector.

## CATALYTIC ACTIVITY TEST

300 mg of the sample with 40-60 mesh was used to evaluate the catalytic oxidation of toluene in a continuous flow fixed-bed tube microreactor (Φ = 6.0 mm). The toluene vapor was generated and injected using a bubbler in a thermostatic bath at 0 ℃, which passed through a container filled with liquid toluene. The reactant mixture (volumetric composition) consisted of 1000 ppm toluene and 20% $O_2$ balanced in $N_2$ with a total flow of 200 mL/min, corresponding to WHSV of 40,000 mL $g^{-1}$ $h^{-1}$. At the beginning of each test, the catalyst was pretreated in the real reactant mixture for 1 h in order to overcome the over-estimation of toluene catalytic combustion conversion caused by adsorption of toluene. The performances at steady states (typically after 0.5 h for every 10 °C) were used for discussion. The concentrations of the reactants and the generation of the catalytic oxidation products were monitored in real time by a GC machine (Shimadzu 2014C) equipped with double flame ionization detectors (FID), where $CO_2$ was detected by $CO_2$ detector.

The toluene conversion ($X_{Toluene}$) and reaction rate r (mol $g^{-1}$ $s^{-1}$) was calculated using the following equations:

$$X_{Toluene}(\%) = (([C_7H_8]_{in} - [C_7H_8]_{out})/[C_7H_8]_{in}) \times 100\% \quad (1)$$

$$r = [C_7H_8]_{in} \times X\%/m_{cat} = WHSV \times X \times 1.240079 \times 10^{-13} \quad (2)$$

where $[C_7H_8]$in and $[C_7H_8]$out denoted the inlet and outlet concentrations of toluene, respectively. where $C_{CO_2}$ is the outlet gas $CO_2$ concentration.

$$X_{CO2} = [CO_2]_{out}/(7[C_7H_8]_{in}) \times 100\% \quad (3)$$

where $[CO_2]_{out}$ is the outlet gas $CO_2$ concentration. This equation is based on the molar ratio of toluene ($C_7H_8$) to $CO_2$ is 1: 7.

## COMPUTATIONAL METHODS

Our spin-polarized DFT calculations have been carried out with the Vienna *Ab initio* Simulation Package (VASP) [1] using the Perdew-Burke-Ernzerhof (PBE) functional [2] and the projector augmented wave (PAW) method [3]. For all calculations, a plane wave energy cutoff of 400 eV was used and the Brillouin zone integration was performed using Monkhorst-Pack scheme with 2 × 2 × 1 k-points [4]. For geometry optimizations, the force and energy convergences were 0.025 eV/Å and $10^{-6}$ eV, respectively. The DFT + U was applied to address the on-site Coulomb interaction with the U-J parameters of 3.3. eV for Co 3d [5]. To account for van der Waals (vdW) interaction, the DFT-D3 method of Grimme was utilized [6].

In this work, the $Co_3O_4$ (311) (1 × 1) slab surface containing 96 Co and 128 O atoms was employed. During geometry optimizations, the bottom 3 Co layers are fixed to their bulk positions and all the rest atoms are fully relaxed. A vacuum space of 15 Å was added in the direction perpendicular to the surface to prevent interactions between periodic images.

The O- and Co-vacancy formation energies ($E_{vac}$) were calculated as: $E_{vac} = E_{slap} - E_{slap\text{-}vac} - E_{removed}$ where $E_{slap}$ is the energy of (311) surface without vacancy site and $E_{slap\text{-}vac}$ and $E_{removed}$ are the energy of (311) surface with O- or Co-vacancy site and the energy of ½($O_2$) for O vacancy or the energy of Co atom for Co vacancy, respectively. And the adsorption energy ($E_{ads}$) of $O_2$ on the $Co_3O_4$ (311) surface with O- and Co-vacancy site were defined by $E_{ads} = E_{O2/slap\text{-}vac} - E_{slap\text{-}vac} - E_{O2}$. Here, $E_{O2/slap\text{-}vac}$ is the energy of adsorption complex and $E_{slap\text{-}vac}$ and $E_{O2}$ are the energy of corresponding slap

surface and isolated oxygen molecule, respectively.

158 **Table S1.** $H_2$ consumption from $H_2$-TPR and catalytic properties of $Co_3O_4$-HA, $Co_3O_4$-

159 MA, and $Co_3O_4$-LA.

160

| | **$H_2$ consumption (mmol/g)** | | | | **$T_{50\%}$/℃** | **$T_{90\%}$/℃** | **Ea/(kJ/mol)** |
|---|---|---|---|---|---|---|---|
| | **$C_{Tmin}$** | **$C_{Tmax}$** | **$C_{Total}$** | **$C_{Tmin/Tmax}$(%)** | | | |
| $Co_3O_4$-HA | 3.4 | 12.2 | 15.6 | 38.6 | 232 | 240 | 35.35 |
| $Co_3O_4$-MA | 3.5 | 8.8 | 12.3 | 66.0 | 242 | 251 | 40.41 |
| $Co_3O_4$-LA | 5.6 | 11.3 | 16.9 | 98.2 | 250 | 260 | 44.74 |

161

162 **Table S2.** Catalytic performance parameters reported on toluene over related catalysts.

| Catalysts | Surface area ($m^2 \cdot g^{-1}$) | VOC conc. (ppm) | GHSV ($mL \cdot g_{cat}^{-1} \cdot h^{-1}$) | $T_{50\%}$ ($^oC$) | $T_{90\%}$ ($^oC$) | References |
|---|---|---|---|---|---|---|
| $Co_3O_4$-HA | 19.4 | 1000 | 40000 | 232 | 240 | This work |
| Pt/KBeta-SDS | 299 | 1000 | 60000 | 142 | 150 ($T_{98}$) | J. Mater. Chem. A. 2015, 3, 5556. |
| 3D hierarchical $Co_3O_4$ | 26.7 | 500 | 60000 | 234 | >245 | Appl. Surf. Sci. 2020, 507, 145. |
| $Co_3O_4$-cube | 83.1 | 1000 | 48000 | 240 | 248 | J. Mater. Chem. A. 2018, 6, 498. |
| 0.99Au/3DOM $Co_3O_4$ | 36.2 | 1000 | 40000 | 268 | 275 | J. Catal. 2015, 322, 38. |
| 6.4Au/bulk $Co_3O_4$ | 8.7 | 1000 | 20000 | 244 | 277 | J. Catal. 2014, 309, 408. |
| $Co_3O_4$-HT | 41.9 | 1000 | 20000 | 241 | 260 | ACS Catal. 2014, 4, 2753. |

163

**Table S3.** Summary of the physicochemical properties of $Co_3O_4$-HA, $Co_3O_4$-MA, and $Co_3O_4$-LA.

| Catalysts | Crystalline/% | Lattice parameter/Å | BET surface area ($m^2g^{-1}$) | $O_{ads}/(O_{ads}+O_{latt})$ (%) | $Co^{3+}/Co^{2+}$ (%) |
|---|---|---|---|---|---|
| $Co_3O_4$-HA | 58.59 | a=b=c=8.067 | 19.4 | 36.6 | 34.0 |
| $Co_3O_4$-MA | 69.07 | a=b=c=8.080 | 14.8 | 32.4 | 40.9 |
| $Co_3O_4$-LA | 73.73 | a=b=c=8.077 | 8.0 | 32.3 | 46.5 |

**Table S4.** Quantitative data of toluene TPD-MS of $Co_3O_4$-HA, $Co_3O_4$-MA, and $Co_3O_4$-LA.

| | $Co_3O_4$-HA | $Co_3O_4$-MA | $Co_3O_4$-LA |
|---|---|---|---|
| T(Toluene)/□ | 73 | 64 | 58 |
| T($CO_2$)/□ | 339 | 341 | 340 |

**Table S5.** Infrared vibration information of toluene related to intermediate species adsorbed on the catalyst.

| Wavenumber($cm^{-1}$) | Vibration mode | References |
|---|---|---|
| 1025 $cm^{-1}$<br>1155 $cm^{-1}$<br>1177 $cm^{-1}$ | The C-O stretching vibration of benzyl alcohol | Appl. Surf. Sci. 2014, 311, 690.<br>Appl. Catal., B. 2016, 181, 236.<br>Chem. Eng. J. 2020, 125192. |
| 1599 $cm^{-1}$ | The benzene ring vibration | Chem. Eng. J. 2015, 270, 58. |
| 1305 $cm^{-1}$ | The vibrational peak of maleic anhydride | Chem. Eng. J. 2018, 334, 768.<br>Appl. Catal., B 2019, 256, 117814.<br>ACS Appl. Mater. Interfaces 2019, 11, 730. |
| 1408 $cm^{-1}$ | C-O symmetric stretching vibration peak attributed to benzoate | Appl. Catal., B 2019, 245, 502.<br>ACS Catal. 2019, 9, 6698.<br>J. Mater. Chem. A 2019, 7, 3366. |
| 1520 $cm^{-1}$ | The anti-symmetric vibration of the COO- group of the benzoate | |
| 1447 $cm^{-1}$ | The vibration of the skeleton C-C bond derived from the benzene ring of benzaldehyde | ACS Catal. 2019, 9, 6698.<br>Chem. Eng. J. 2018, 344, 469.<br>Appl. Catal., B 2018, 224, 705. |
| 1468 $cm^{-1}$<br>1654 $cm^{-1}$<br>1753 $cm^{-1}$ | The C=O vibration peak subordinate to benzaldehyde | |

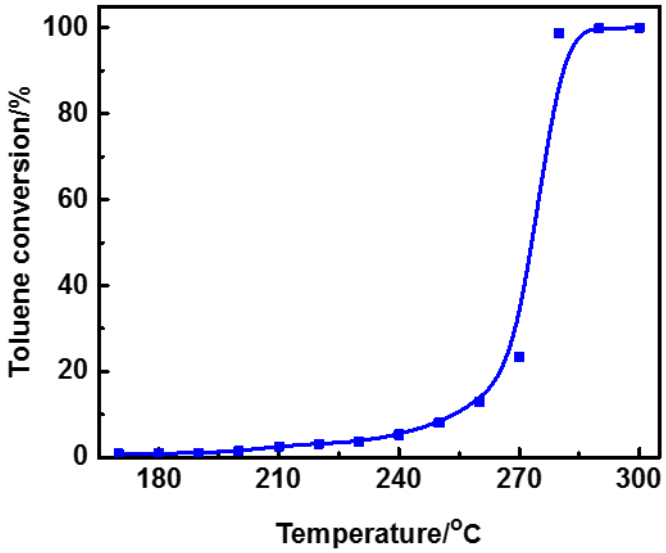


172

173 **Figure S1.** Plots of toluene conversion versus temperature over $Co_3O_4$-600.

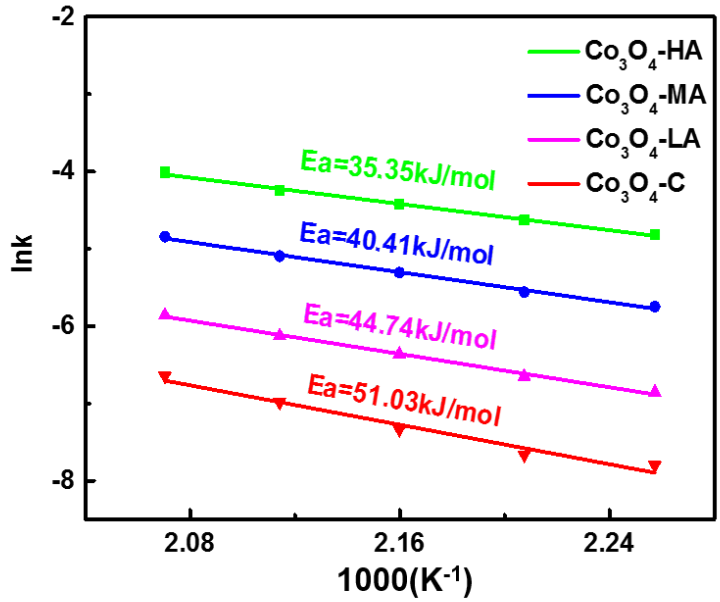


174

175 **Figure S2.** Arrhenius plots for toluene oxidation over $Co_3O_4$-HA, $Co_3O_4$-MA, $Co_3O_4$-

176 LA, and $Co_3O_4$-C.

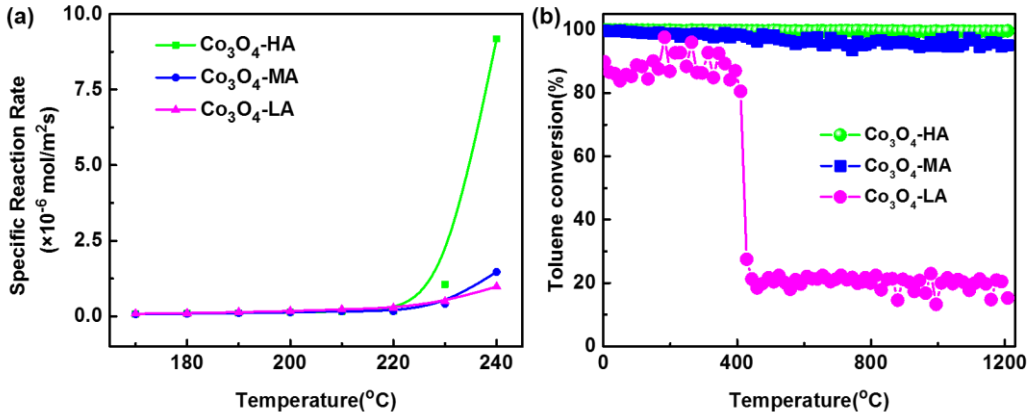


177

178 **Figure S3.** (a) Plots of specific reaction rate of different samples normalized by specific

179 surface area, and (b) catalytic stability (under 250°C for 20h) of $Co_3O_4$-HA, $Co_3O_4$-MA,

180 and $Co_3O_4$-LA.

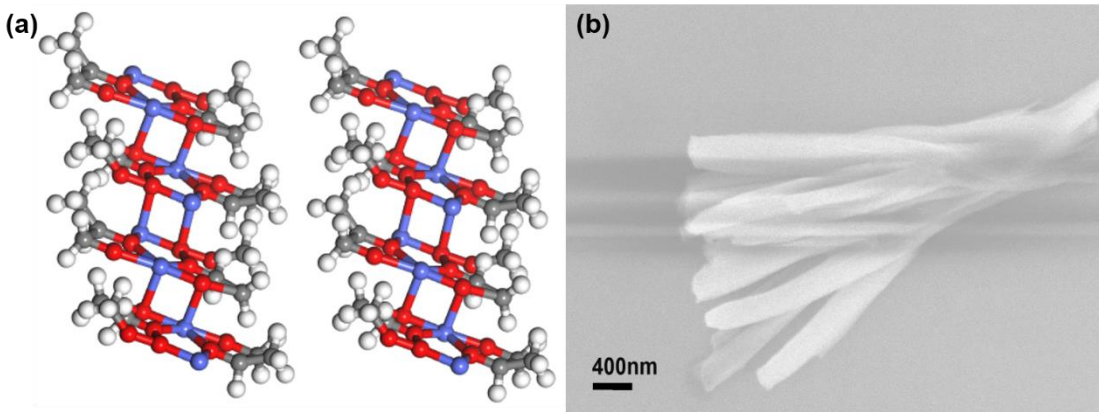


**Figure S4.** (a) Crystal structure and (b) SEM image of $Co_3O_4$ precursor.

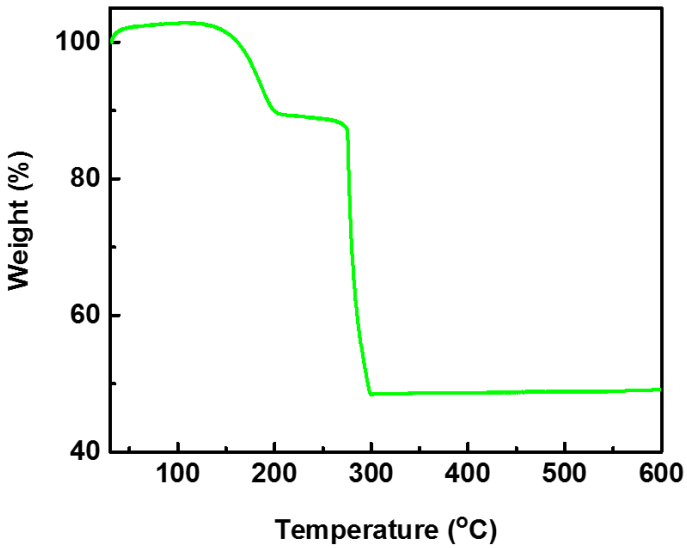


**Figure S5.** TG profiles of CoGly (precursor).

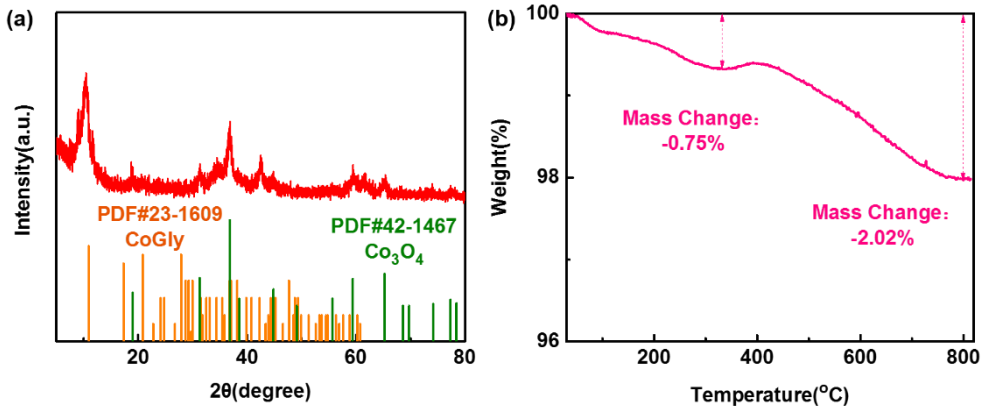


**Figure S6.** (a) XRD patterns and (b) TG profiles of $Co_3O_4$-C.

**Note:** $Co_3O_4$-C is a mixed phase of carbon and cobalt oxide; the crystal plane index is not good to be directly marked on the XRD pattern. However, combined with the synthesis method in the article, as shown in Figure S6a, two PDF cards can explain the XRD pattern of $Co_3O_4$-C. CoGly (PDF#23-1609)[7] is a precursor to synthetic catalysts and contains cobalt and glycerin. $Co_3O_4$ (PDF#42-1467) is the product after calcination. These indicate that, CoGly has not been completely calcined under air calcination at 270 °C, and the product contains part of GoGly and $Co_3O_4$. The thermogravimetric experiment was carried out over $Co_3O_4$-C to prove the amount of $Co_3O_4$ in $Co_3O_4$-C catalyst. It can be seen from Figure S6b that the curve has a small platform in the temperature range of 300-400°C, and the mass loss is 0.75% at this time. This loss is due to the consumption of carbon species in $Co_3O_4$-C. The mass loss (1.27%) after 400 °C may be regarded as the oxygen released during the sintering of small particles into large particles. It can be concluded that the loading of $Co_3O_4$ in $Co_3O_4$-C is around 99.18%.

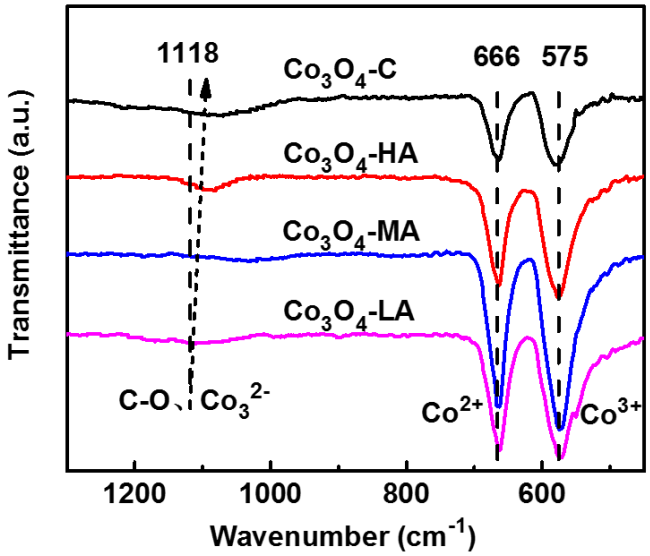


**Figure S7.** FTIR spectra of $Co_3O_4$-C, $Co_3O_4$-HA, $Co_3O_4$-MA, and $Co_3O_4$-LA.

**Note:** The peak at 575 $cm^{-1}$ is regarded as the peak of $Co^{3+}$, the peak at 666 $cm^{-1}$ is classified as the peak of $Co^{2+}$, and the peak at 1118 $cm^{-1}$ is attributed to the vibration of C-O and $CO_3^{2-}$.[8] Obviously, all samples have peaks related to $Co^{3+}$ and $Co^{2+}$ species, which indicates that all samples contain the crystal phase of $Co_3O_4$. Although all samples have peaks at 1118$cm^{-1}$, the attribution varies. The presence of this peak in $Co_3O_4$-C is attributed to the relatively uniform distribution of carbon species in $Co_3O_4$-C (XRD and Raman of $Co_3O_4$-C can be proven again.), while the remaining samples containing this peak is considered to be a little $CO_3^{2-}$ remaining on the sample when the precursor is calcined.

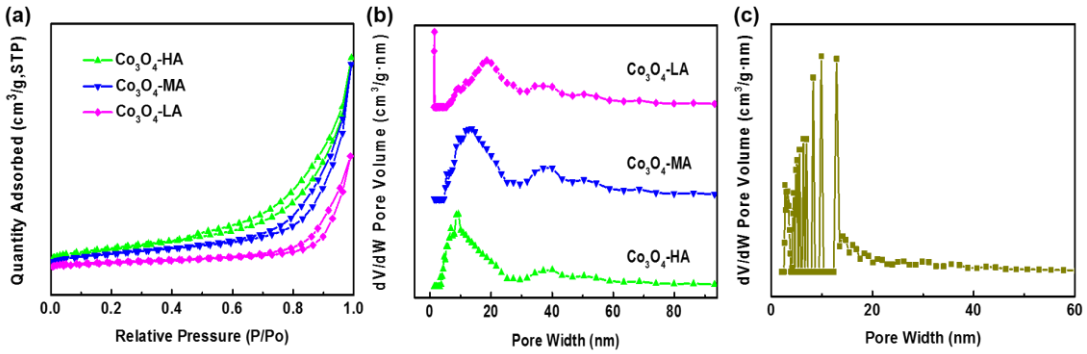


**Figure S8.** (a) $N_2$ adsorption-desorption isotherms, and (b) pore size distribution profiles of $Co_3O_4$-HA, $Co_3O_4$-MA, and $Co_3O_4$-LA. (c) The pore size distribution profile of $Co_3O_4$-C.

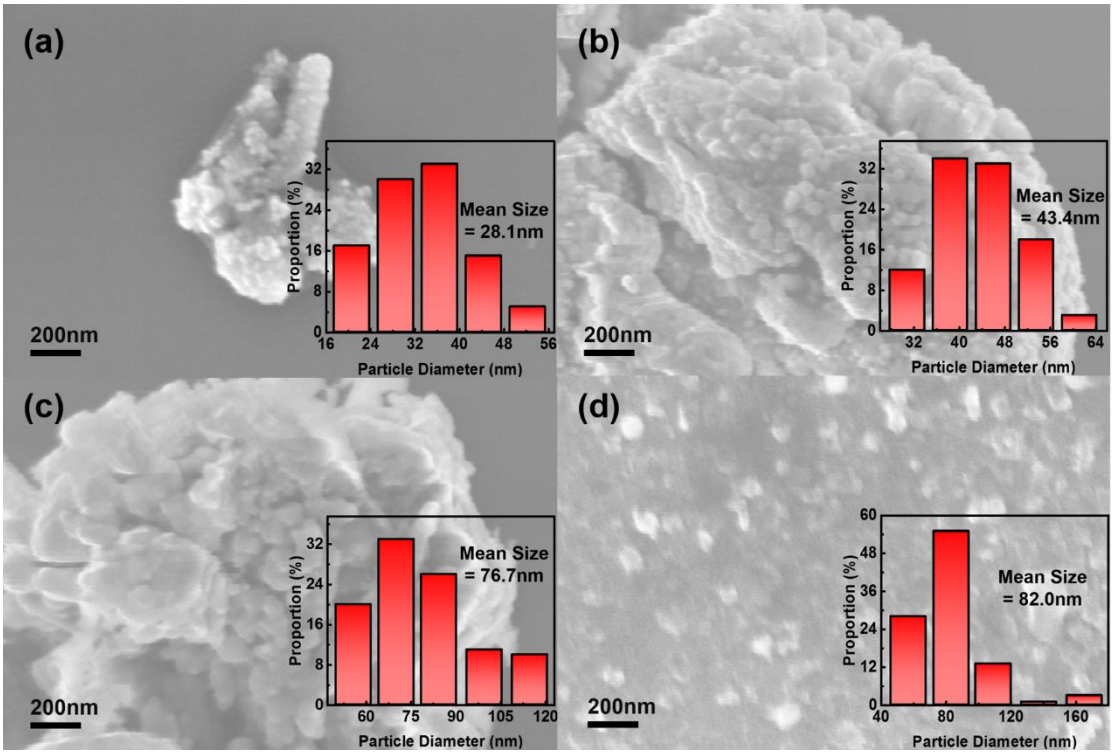


**Figure S9.** SEM images of (a) $Co_3O_4$-HA, (b) $Co_3O_4$-MA, (c) $Co_3O_4$-LA, and (d) $Co_3O_4$-C.

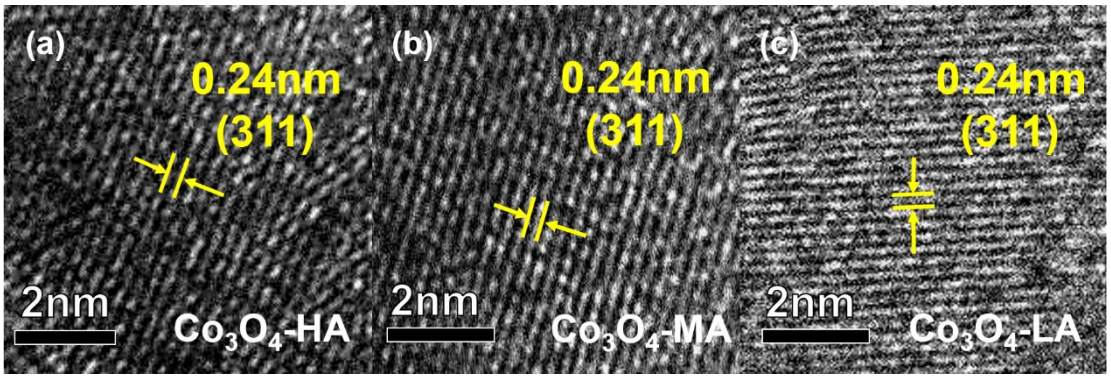


**Figure S10.** HRTEM images of (a) $Co_3O_4$-HA, (b) $Co_3O_4$-MA, and (c) $Co_3O_4$-LA.

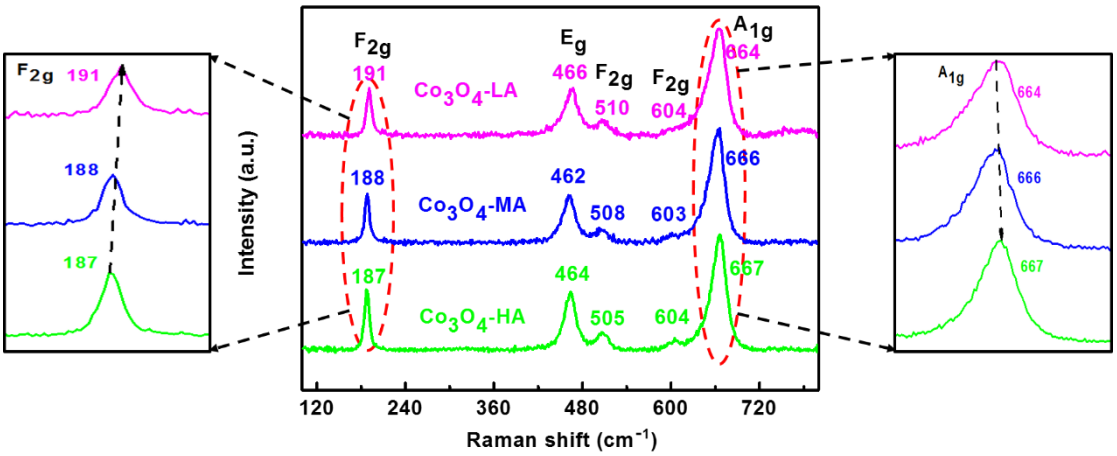


222

223 **Figure S11.** Raman spectra of the $Co_3O_4$-HA, $Co_3O_4$-MA, and $Co_3O_4$-LA.

224

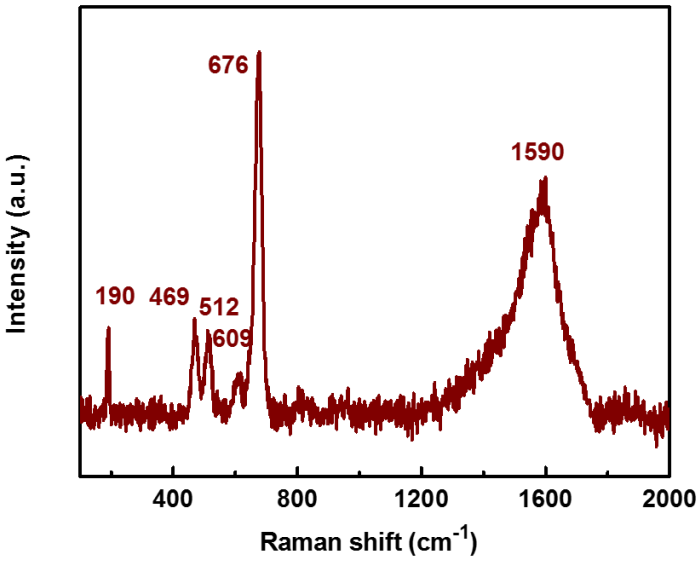


**Figure S12.** Raman spectra of $Co_3O_4$-C.

**Note:** As shown in Figure S12, the peaks at 190cm$^{-1}$ ($F_{2g}$), 469 cm$^{-1}$, ($E_g$), 512 cm$^{-1}$ ($F_{2g}$), 609 cm$^{-1}$ ($F_{2g}$), and 676 cm$^{-1}$ ($A_{1g}$) are assigned to the Raman active vibration mode of $Co_3O_4$.[9] The peak at 190cm$^{-1}$ is attributed to four-coordinated Co ($CoO_4$), and the peak at 676cm$^{-1}$ is attributed to six-coordinated Co ($CoO_6$). In addition, the peak at 1590 cm$^{-1}$ is assigned to the G-band peak of the carbon peak. In summary, $Co_3O_4$-270 is a mixed-phase catalyst containing a part of $Co_3O_4$ crystal phase and carbon species.

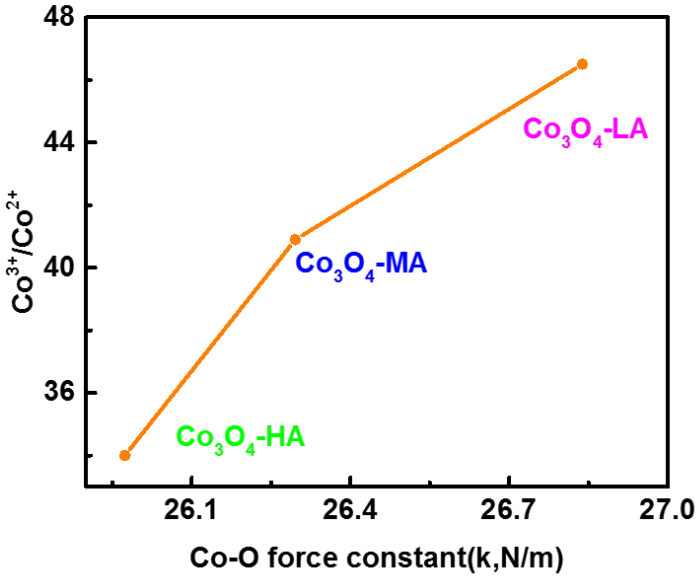


233

234 **Figure S13.** The trend profile of the relationship between the ratio of $Co^{3+}$ to $Co^{2+}$ from

235 XPS results and the Co−O bond force constant from Raman results of the catalysts.

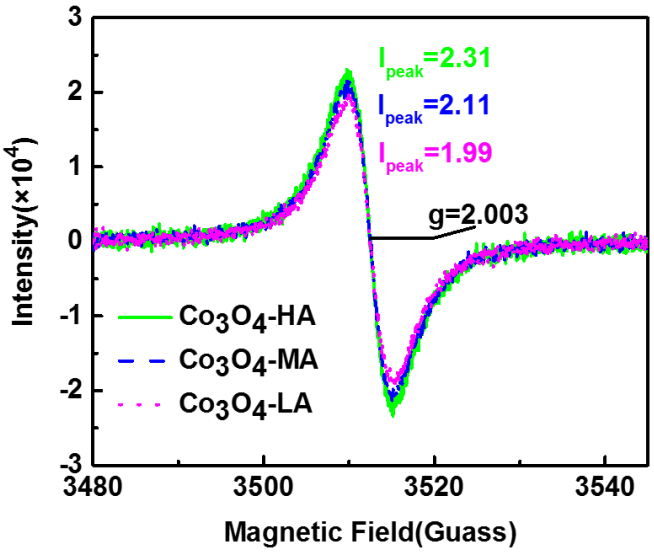


236

237 **Figure S14.** EPR spectra of the $Co_3O_4$-HA, $Co_3O_4$-MA, and $Co_3O_4$-LA.

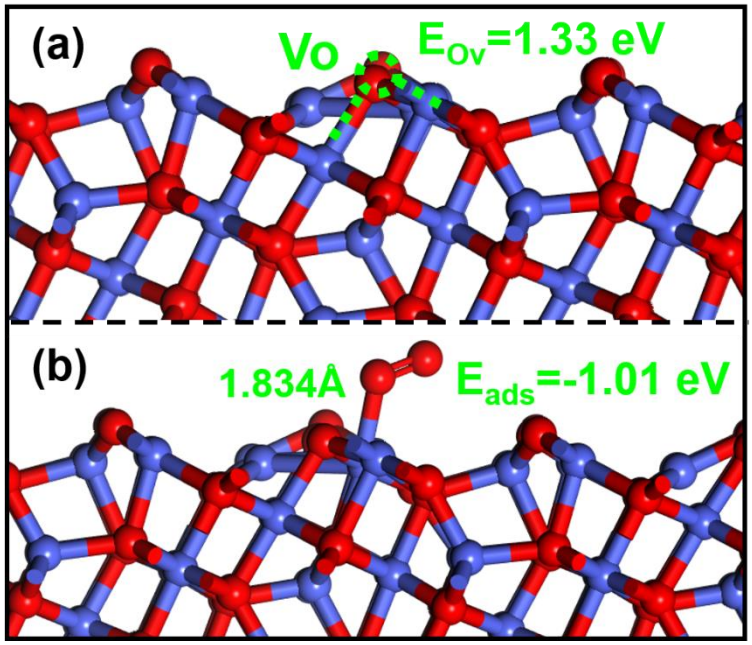


**Figure S15.** Optimized structures of (a) oxygen vacancy and (b) $O_2$ adsorption on low activated $Co_3O_4$.

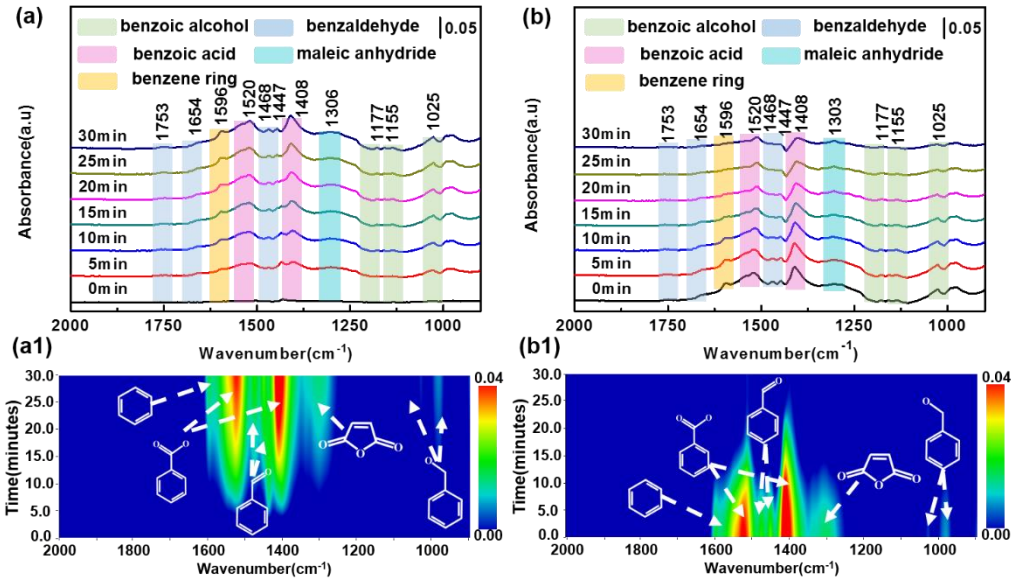


241

242 **Figure S16.** In situ DRIFTS spectra of toluene (a, a1) adsorption and (b, b1) oxidation

243 on $Co_3O_4$-MA at 240 °C.

244

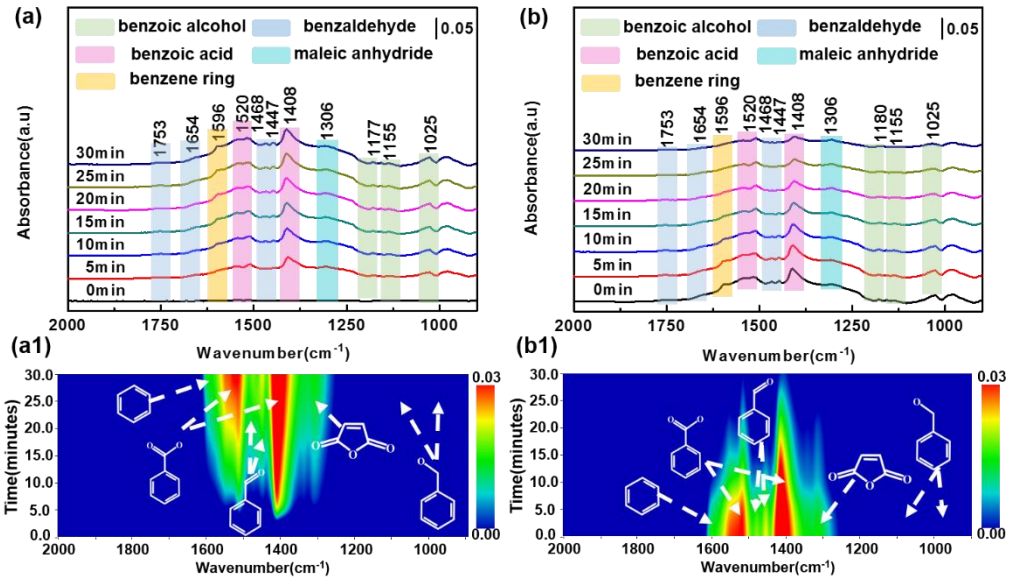


245

246 **Figure S17.** In situ DRIFTS spectra of toluene (a, a1) adsorption and (b, b1) oxidation

247 on $Co_3O_4$-LA at 240 °C.

248

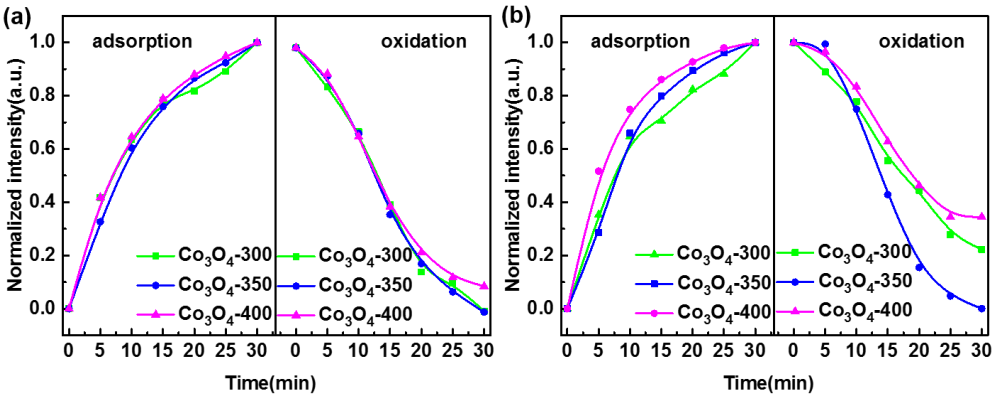


249

250 **Figure S18.** Accumulation and consumption of (a) benzyl alcohol and (b) benzaldehyde

251 upon passing air stream over the $Co_3O_4$ catalysts after the catalysts absorbed toluene

252 for 30 min.

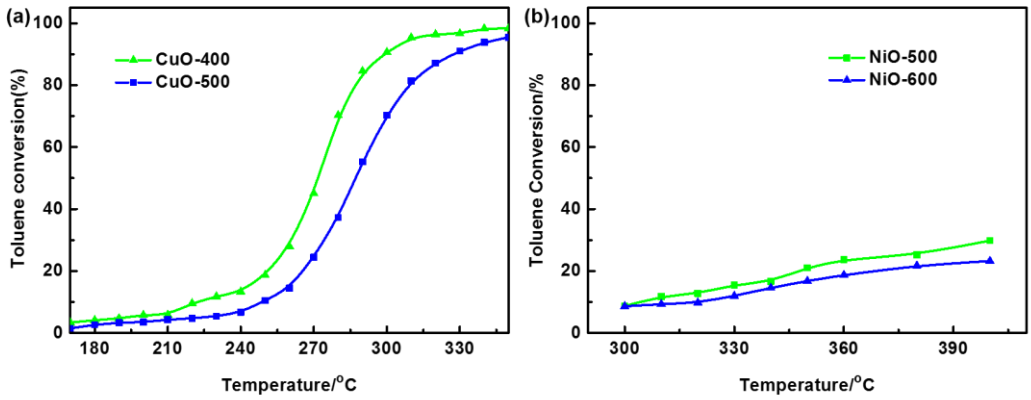


**Figure S19.** Plots of toluene conversion versus temperature over (a) CuO and (b) NiO catalysts. (The number represents the processing temperature.)

**Note:** CuO and NiO have better toluene degradation performance at lower pyrolysis temperature. The bond strength between CuO and NiO metal and oxygen needs to be further explored in future work.

## REFERENCES


(1) G. Kresse, J. Furthmüller, Efficient iterative schemes for ab initio total-energy calculations using a plane-wave basis set, *Phys. Rev. B* 54 (16) (**1996**) 11169–11186.

(2) J.P. Perdew, K. Burke, M. Ernzerhof, Generalized gradient approximation made simple, *Phys. Rev. Lett*. 77 (18) (**1996**) 3865–3868.

(3) G. Kresse, D. Joubert, From ultrasoft pseudopotentials to the projector augmented-wave method, *Phys. Rev.* B 59 (3) (**1999**) 1758–1775.

(4) H.J. Monkhorst, J.D. Pack, Special points for Brillouin-zone integrations, *Phys. Rev. B* 13 (12) (**1976**) 5188–5192.

(5) S.L. Dudarev, G.A. Botton, S.Y. Savrasov, C.J. Humphreys, A.P. Sutton, Electron-energy-loss spectra and the structural stability of nickel oxide: An LSDA+U study, *Phys. Rev. B* 57 (**1998**) 1505-1509.

(6) Grimme S., Antony J., Ehrlich S., Krieg H., A consistent and accurate ab initio parametrization of density functional dispersion correction (DFT-D) for the 94 elements H-Pu, *J. Chem. Phys.* 132 (**2010**) 154104.

(7) Lau, P. C.; Kwong, T. L.; Yung, K. F., Effective heterogeneous transition metal glycerolates catalysts for one-step biodiesel production from low grade non-refined Jatropha oil and crude aqueous bioethanol. *Sci. Rep.* 2016, 6, 23822.

(8) Xu, H.; Hai, Z.; Diwu, J.; Zhang, Q.; Gao, L.; Cui, D.; Zang, J.; Liu, J.; Xue, C., Synthesis and Microwave Absorption Properties of Core-Shell Structured Co3O4-PANI Nanocomposites. *J. Nanomater.* 2015, 2015, 1-8.

(9) Bae, S.-H.; Kim, J.-E.; Randriamahazaka, H.; Moon, S.-Y.; Park, J.-Y.; Oh, I.-K.,

281 Seamlessly Conductive 3D Nanoarchitecture of Core-Shell Ni-Co Nanowire Network
282 for Highly Efficient Oxygen Evolution. *Adv. Energy Materials.* 2017, 7, (1), 1601492.